

## Impact of an antidote vacancy on the electronic and transport properties of germanene nanoribbons: A first principles study

Azam Samipour<sup>a</sup>, Daryoosh Dideban<sup>b,a,\*</sup>, Hadi Heidari<sup>c</sup>

<sup>a</sup> Institute of Nanoscience and Nanotechnology, University of Kashan, Kashan, Iran

<sup>b</sup> Department of Electrical and Computer Engineering, University of Kashan, Kashan, Iran

<sup>c</sup> James Watt School of Engineering, University of Glasgow, Glasgow, UK



### ARTICLE INFO

#### Keywords:

Germanene nanoribbon  
Antidote vacancy  
Semiconductor defects  
Electronic properties  
Quantum transport

### ABSTRACT

In this article, we investigate the effect of various antidote defects on the electronic properties and current characteristics of an armchair Germanene nanoribbon (AGeNR) using density functional theory (DFT) and non-equilibrium Green's function (NEGF) method. The defected AGeNRs are introduced by setting antidote topologies in the pristine nanoribbons, resulting in antidote super-lattice of AGeNRs. It is found that new electronic properties appear due to the presence of defects. The obtained results indicate that bandgap of the defected AGeNRs can be increased or decreased in different cases. Moreover, the transport properties are analyzed based on the various defect locations in the AGeNR when the ribbon is utilized as the channel of a tunneling field effect transistor (TFET). Based on our results, it is found that the presence of antidote defects leads to reduction or increase in the current, drifting the Dirac point, and decreasing or increasing the minimum or off-state current.

### 1. Introduction

Since 2004, graphene has attracted considerable attention because of its unique structural, electronic and mechanical properties and is considered as a candidate for future electronic nano-scale devices [1–9]. However, graphene as the two dimensional (2D) material has a zero bandgap resulting in undesirable limitations in semiconductor device applications. In electronic devices, semiconductors with a tunable bandgap are required [10–17]. To overcome this issue, several methods such as application of strain [18,19], adsorption of suitable elements [20,21], utilizing nanoribbons of graphene [9,17,22–24], application of an external potential [25,26], layered stacking [27,28], Doping with other elements such as Boron and Nitrogen [8,9,29] and creation of defects such as antidotes [9,30,31] are among the methods which have been proposed in the literature.

After the discovery of graphene, looking for other 2D materials has been increased. Among the two-dimensional materials, Because of the similarity of silicene and germanene to graphene, special attention has been paid to these materials [32–35]. These materials have same honeycomb structure as graphene but graphene presents  $sp^2$  hybridized carbon atoms and a planar configuration whereas silicene and germanene due to the mixture of  $sp^2$  and  $sp^3$  hybridization have low-buckled

structure. The presence of buckling in these materials leads to the increased chemical reactivity. Moreover, in silicene and germanene, bandgap control is possible by using an external electric field [6,36,37].

After the synthesis of silicene on many surfaces during the years 2010–2013, germanene was also successfully synthesized on Ag (111), Al (111) and Pt (111) surfaces. During the synthesis process, the presence of structural defects is unavoidable; hence it is necessary to examine the influence of defects on the structural, electronic and transport properties of these materials [12,13,37,38].

Antidotes are important nanostructures for the new generation of nanoelectronic and spintronic devices. They can be utilized to change the band structure and energy bandgap depending on their position and geometry and create desired electronic properties. This change is due to strong quantum confinement of the lattice in presence of antidotes. Based on the literature, antidotes change the electronic properties of graphene and silicene nanoribbons from semiconducting to metallic or vice versa. They can also be utilized to tune the bandgap of a nanoribbon [13,39,40]. In this article, was theoretically examine the influence of different antidote topologies on the electronic properties and current characteristics of pristine armchair germanene nanoribbons (AGeNR) of different widths.

Four different topologies are considered in our study. Moreover, to

\* Corresponding author. Department of Electrical and Computer Engineering, University of Kashan, Kashan, Iran.  
E-mail address: [dideban@kashanu.ac.ir](mailto:dideban@kashanu.ac.ir) (D. Dideban).

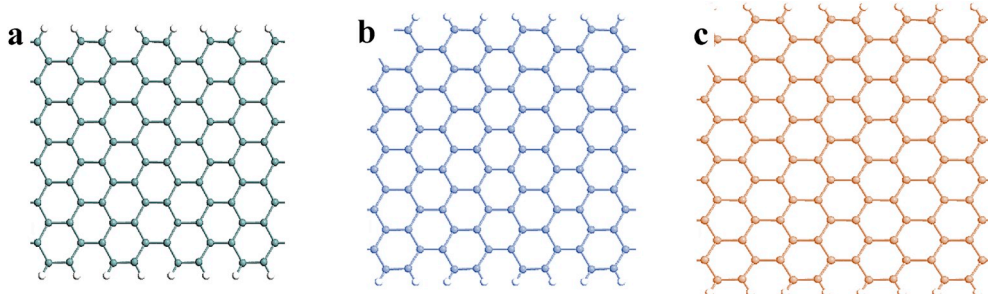


**Fig. 1.** Top views of the optimized structures: (a) 12-AGeNR supercell; (b) 13-AGeNR supercell; (c) 14-AGeNR supercell.

analyze the physical behaviors, electronic properties and current characteristics of these defected nanoribbons are compared with a pristine germanene nanoribbon for each case. The rest of this research is organized as follows: In section 2, the device structure and simulation setup is presented and discussed in details. Section 3 is devoted to the results but is divided in two sub-sections. In the first subsection, the impact of different antidote topologies on the band structure is revealed. In the second subsection, we analyze the influence of aforementioned antidotes on the current characteristics of AGeNRs. The paper is concluded in section 4.

## 2. Device structure and simulation setup

The simulation procedure was performed in three steps. Initially, the unit cell of a pristine AGeNR was constructed and fully relaxed. Afterward, an antidote vacancy was introduced by removing the atoms from the pristine center supercell. In this step, the impact of antidotes on the nanoribbon band structure was investigated. Finally, effect of antidotes on GeNR-TFET device characteristics was studied.

The optimization of geometry and calculation of the electronic structure of the AGeNR (the first two steps) are carried out using first principles calculations based on density functional theory (DFT). The generalized gradient approximation (GGA) is utilized for exchange-correlation functional of Perdew, Burke and Ernzerhof (PBE) [11,12,19]. The atomic orbital basis sets of double-j plus polarization orbitals (DZP) are used. Periodic boundary conditions with two vacuum layers of approximately 15 Å in x-direction and 25 Å in y-direction are employed to prevent undesired image-image interaction. The cut off energy is set to 75 Hartrees and the Brillouin zone sampling is performed by Monkhorst-Pack (MP) k-point with a mesh of (1\*1\*41) for optimization of geometry and mesh of (1\*1\*101) for electronic properties of the primitive unit cell and the supercell. Geometry optimization is performed until the residual forces threshold became smaller than 0.01 eV/Å. To remove the dangling bond effects on the surface of nanoribbons, edges on both sides were passivated with hydrogen atoms [41, 42]. It is worth noting that hydrogen atoms are also added to saturate dangling bonds at the antidote points.

In AGeNRs the bandgap size is depending on the width of the ribbons. This means that different bandgap sizes are obtained at various width of the ribbon. Considering this dependency, they are divided into three families comprised of  $N = 3m$ ,  $N = 3m + 1$  and  $N = 3m + 2$  where  $N$  is the number of atoms along the ribbon width and  $m$  is an integer. In this way, we examine the electronic properties of three families when they become defective. Widths of 12, 13, and 14 atoms are selected as representations for ribbon widths of  $N = 3m$ ,  $3m + 1$  and  $3m + 2$ , respectively. The considered supercell for this article is  $L = 4$  (the number of unit cell in the direction of length). Schematic view of AGeNR superlattice is shown in Fig. 1. The supercells contain 96 ( $W = 12$ ), 104 ( $W = 13$ ) and 112 ( $W = 14$ ) atoms for the pristine germanene nanoribbons. Also the bond length of Ge-Ge and parameter of buckling was obtained 2.4 Å and  $\Delta = 0.67$  Å respectively.

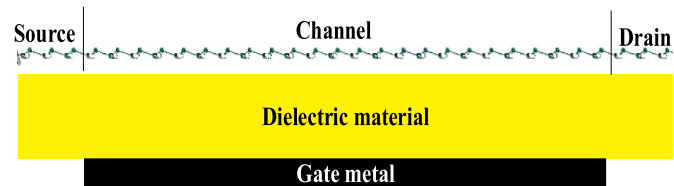


**Fig. 2.** Schematic of a simulated GeNR-TFET.

To obtain I-V characteristics, the non-equilibrium Green's function method is used that is expressed as:

$$I(V_g, V_{bias}) = \frac{2e}{h} \int_{-\infty}^{+\infty} \{ Tr[\Gamma_L G^R \Gamma_R G^A] [f_L(E - \mu_L) - f_R(E - \mu_R)] \} dE$$

where  $e$ ,  $h$ ,  $\Gamma$ , denote the electron charge, Planck's constant, contact and broadening function electrodes, respectively.  $f_{L/R}$  and  $\mu_{L/R}$  represent Fermi-Dirac distribution function for left/right electrodes and the corresponding chemical potential for those electrodes.  $G$  is the Green's function of device which is given by:

$$G_d = (E - H_d - \sum_L - \sum_R)^{-1}$$

where  $E$ ,  $H_d$  and  $\Sigma_{L/R}$  are the carrier energy, device Hamiltonian the self-energy of left/right electrodes, respectively [1,26]. Fig. 2 shows the simulated device for this research. The device is comprised of three parts, i.e. source, channel and drain regions along the z-direction. These three regions are made from an armchair GeNR. The Channel length is 7 nm and the source and drain lengths are the same and equal to 7.04 Å. The gate insulator is  $\text{HfO}_2$  ( $K = 25$ ) with 1 nm thickness and the gate metal thickness is 0.5 nm. The gate insulator covers the entire nanoribbon but the gate metal only covers the channel. P-type and n-type dopants are introduced into source and drain regions, respectively, whereas the channel is intrinsic. The utilized power supply voltage is  $V_D = 0.3$  V. An arbitrary value of zero energy level has been selected as the Fermi level in the band structure and the temperature has been set at  $T = 300$  K.

To investigate the effect of defect position on the band structure, three regions are considered namely close to the source, middle of the channel and close to the drain to introduce the defect. Also in the present work, five different antidote topologies, which are illustrated in Fig. 3, are considered. To obtain the results, ATK software from QuantumWise [43] was used to perform the numerical computations.

## 3. Results and discussion

This section contains two subsections. In the first subsection, the effect of antidote topologies on the band structures of AGeNRs with different number of atoms along the width is discussed. In the second

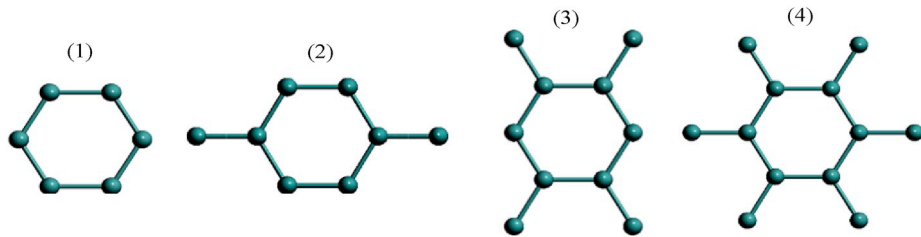


**Fig. 3.** Four different examined antidote topologies introduced as antidote vacancy in armchair germanene nanoribbons.

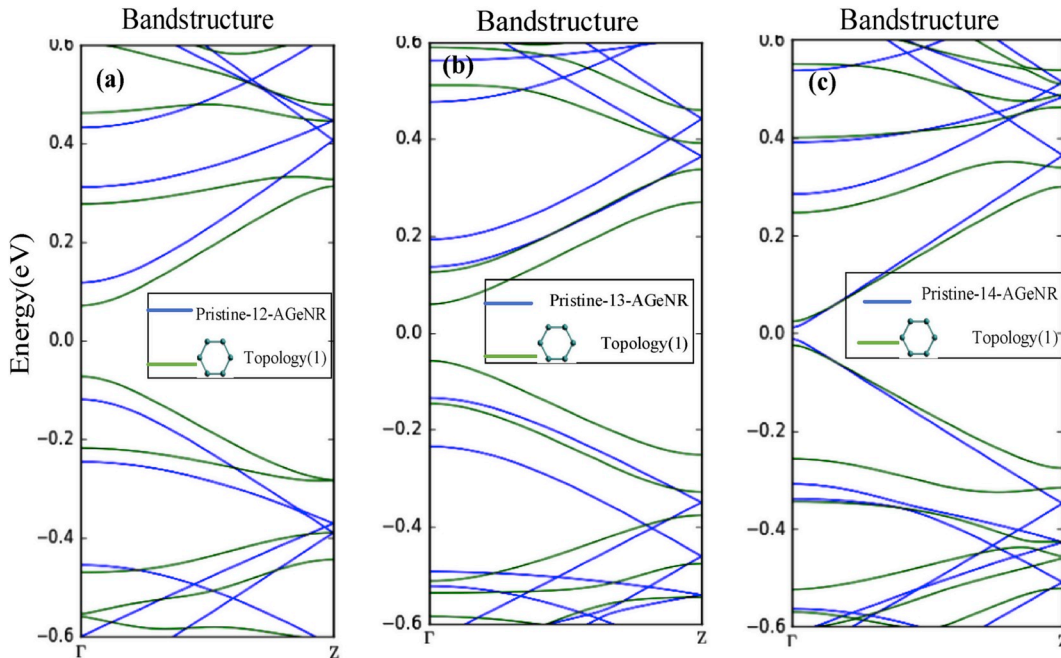


**Fig. 4.** Energy band structure of AGeNR for pristine and defective with antidotes of the type topology 1 for (a)  $N = 12$  (b)  $N = 13$  (c)  $N = 14$ .

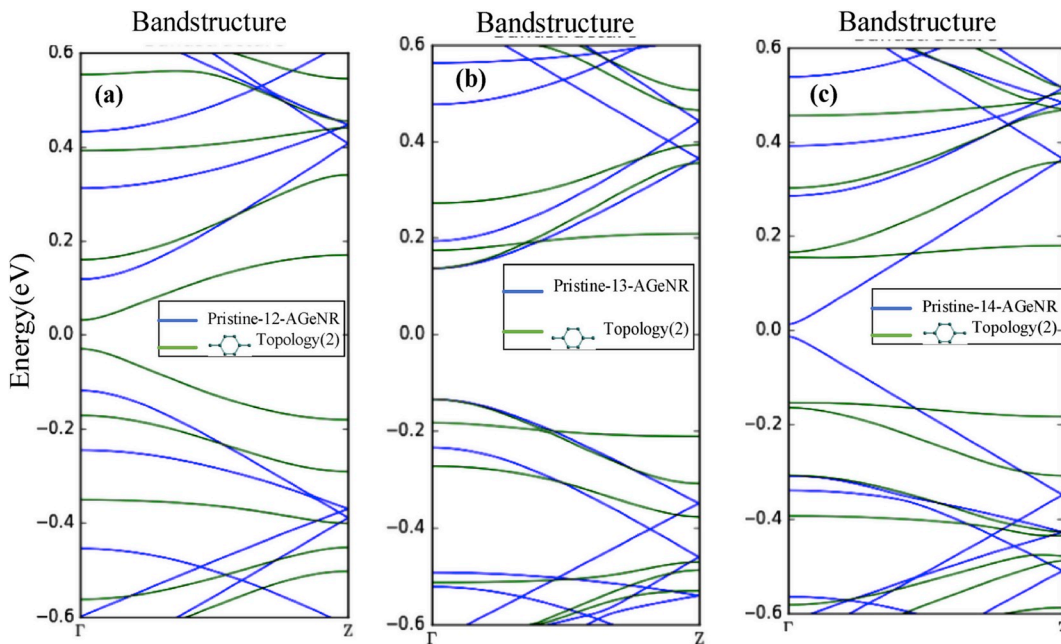


**Fig. 5.** Energy band structure of AGeNR for pristine and defective with antidotes of the type topology 2 for (a)  $N = 12$  (b)  $N = 13$  (c)  $N = 14$ .

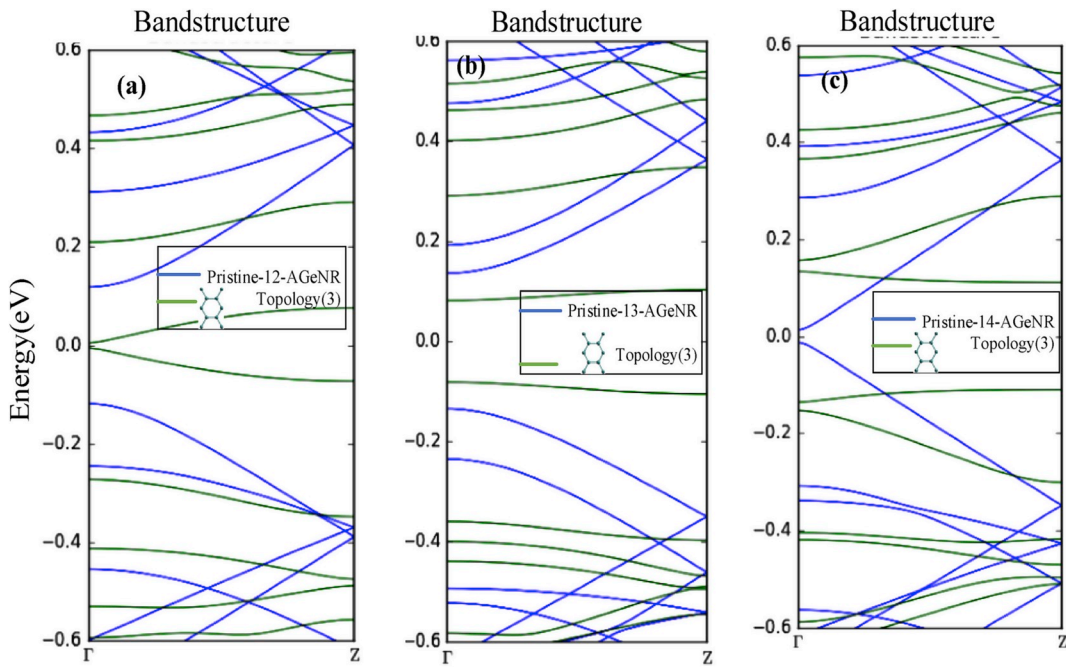


**Fig. 6.** Energy band structure of AGeNR for pristine and defective with antidotes of the type topology 3 for (a) N = 12 (b) N = 13 (c) N = 14.

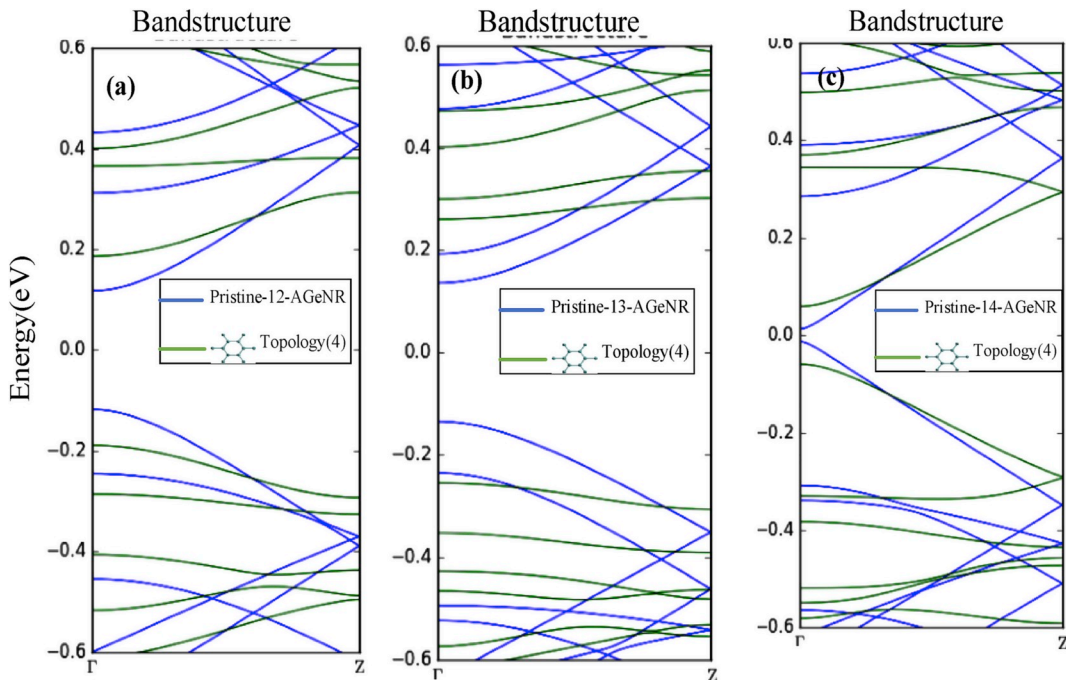


**Fig. 7.** Energy band structure of AGeNR for pristine and defective with antidotes of the type topology 4 for (a) N = 12 (b) N = 13 (c) N = 14.

part, we examine the impact of antidote topologies on the transfer characteristics of TFETs made from mentioned AGeNRs. Also in this subsection, we investigate the electronic properties and transfer characteristics changing the position of the antidote (topology1) along the width of 12-AGeNR.

### 3.1. Impact of antidote topologies on the band structure

Fig. 4 shows the impact of topology (1) defect on the band structure for 12, 13, and 14 atoms along the nanoribbon width. The band

structures of the pristine (non-defective) GeNRs are shown as a reference. The bandgap value of pristine case for 12, 13 and 14-AGeNR is 0.235 eV, 0.26 eV and 0.025 eV, respectively. By introducing topology (1) antidote vacancy, the band gap values will be changed, as shown in Fig. 4. The results obtained from simulations show that the bandgap values are 0.1145 eV for 12-AGeNR, 0.12 eV for 13-AGeNR and 0.05 eV for 14-AGeNR. It can be seen that for 12 and 13-AGeNR, the band gap size is decreased to smaller values while the size of band gap for 14-AGeNR is slightly increased by the presence of this type of defect.

The effects of topology(2)antidote vacancy on the band structures of

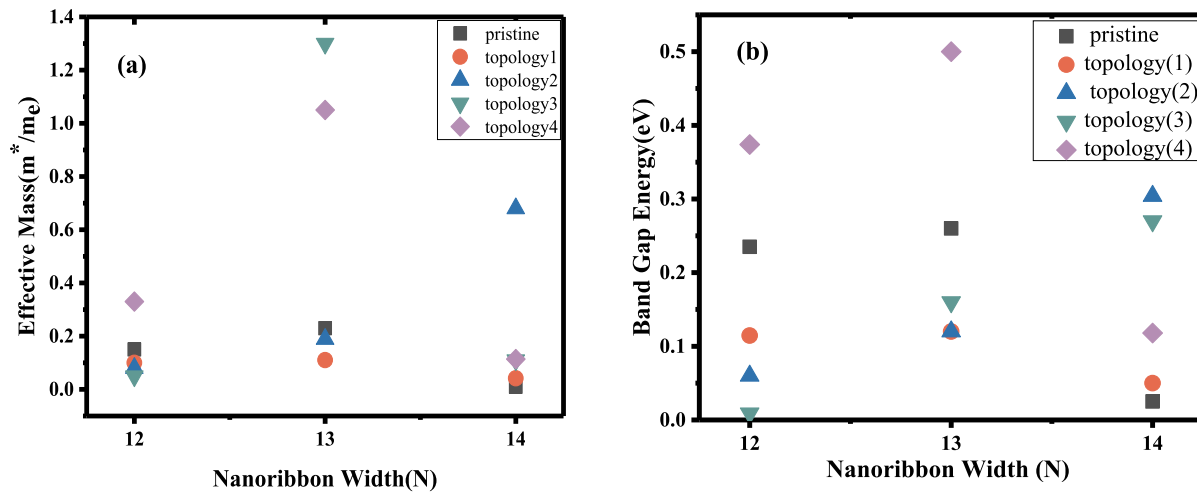


**Fig. 8.** (a) electron effective mass versus number of atoms along the nanoribbon width (N); (b) bandgap versus number of atoms along the nanoribbon width (N) for pristine and defected topologies.

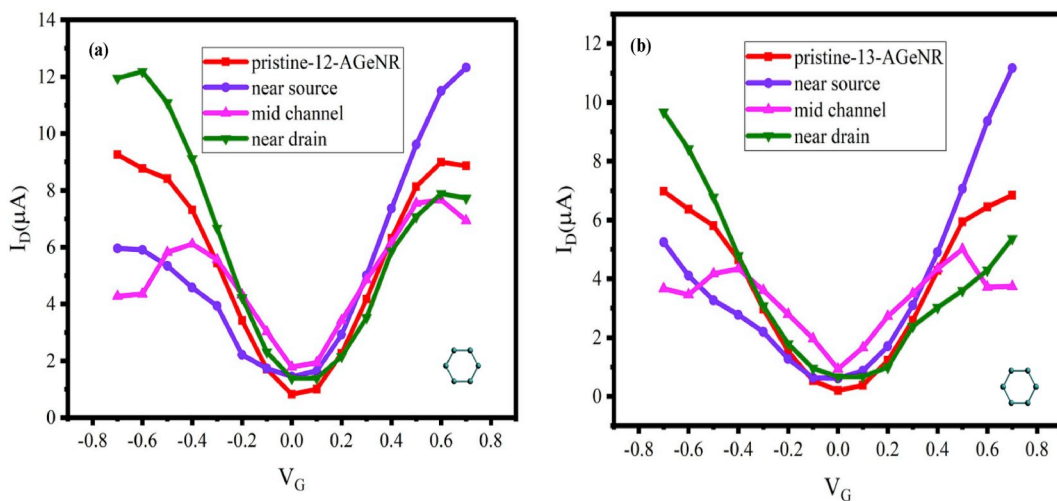
AGeNRs are illustrated in Fig. 5. The band gap size of 0.06 eV, 0.12 eV and 0.304 eV were obtained for 12, 13 and 14-AGeNRs in the presence of this type of antidote defect. As shown in Fig. 5(a,c), the bandgap size of 12-AGeNR has significantly decreased while the size of the bandgap increases significantly for 14-AGeNR. The bandgap value of 13-AGeNR (Fig. 5(b)) is less altered in this case compared with other widths.

Fig. 6 exhibits the influence of topology type (3) antidote vacancy on the band structures of the nanoribbons under study. According to the results, the obtained band gap size in corresponding to 12, 13 and 14 atoms along the width are 0.0093 eV, 0.16 eV, and 0.27 eV, respectively. It can be seen that this type of antidote vacancy causes enhancement of the bandgap to a larger value for 14-AGeNR whereas it shows significant reduction in the bandgap value for 12-AGeNR. This type of antidote turns the 12-AGeNR to behave like metals. Moreover, this antidote decreases the bandgap value in comparison with pristine structure for 13-AGeNR.

The effects of topology (4) on the band structures of AGeNRs in comparison with that of pristine case are illustrated in Fig. 7. As shown in Fig. 7, this kind of antidote results in bandgap incremental trends for all three widths. The associated bandgap values are 0.374 eV, 0.5 eV, and 0.118 eV for 12, 13, and 14-AGeNR, respectively.

It is worth noting that due to the presence of antidotes in all three widths the sub-band patterns are modified and the degeneration of states is broken. It can be concluded that the defects lead to altered electronic properties due to the creation of new quantum confinement in the ribbons. Therefore, the band gap value can be adjusted to a desired value by selecting an appropriate topology of antidote vacancy.

In order to better illustrate important electronic properties of AGeNRs subjected to antidotes, we extracted the electron effective mass and the bandgap from Figs. 4–7. Fig. 8(a) shows the electron effective mass related to free electron effective mass ( $m^*/m_e$ ) for different structures under study versus the number of atoms along the width. As can be seen in Fig. 8(a), the electron effective mass shows significantly higher values in nanoribbons having  $N = 13$  subjected to antidotes of topology 3 and 4. For nanoribbons with  $N = 12$ , only topology 4 causes a boost of  $m^*/m_e$  from 0.1 to 0.35. Finally, in the case of  $N = 14$ , only antidotes of topology 2 makes an increased value of  $m^*/m_e$  from 0.05 to 0.7 and other types of antidotes make slight change in the effective mass. To end this subsection, variation in bandgap energy ( $E_g$ ) versus ribbon width (N) for pristine and defected AGeNRs is shown in Fig. 8(b). It can be seen that  $E_g$  versus N presents an increasing trend for nanoribbons subjected to antidotes of topology 2 and 3. For pristine and topology 4



**Fig. 9.** Current-voltage characteristics of AGeNR-TFET subject to topology 1 antidote defect at different locations in the channel; (a)  $N = 12$  (b)  $N = 13$ .

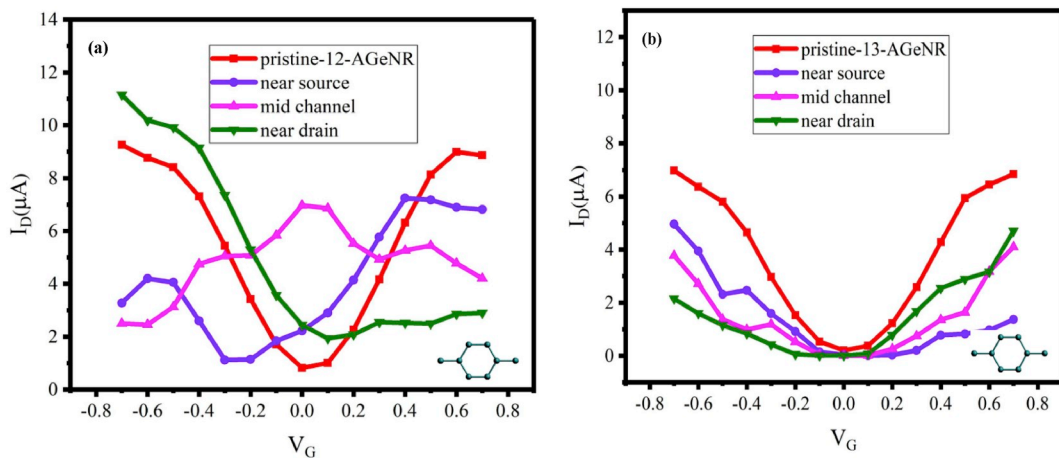


**Fig. 10.** Current-voltage characteristics of AGeNR-TFET subject to topology 2 antidote defect at different locations in the channel; (a)  $N = 12$  (b)  $N = 13$ .

cases, the maximum bandgap occurs at  $N = 13$ . For both latter cases,  $N = 12$  shows a reduced bandgap and  $N = 14$  has the lowest bandgap compared with other widths. It is worth noting that the bandgap value for the pristine case is in agreement with the previous works presented in Refs. [44,45].

### 3.2. Impact of antidote topologies on the transport properties

In this subsection, the current-voltage characteristics of TFETs are investigated for the pristine and defective structures. In this part, the current-voltage characteristics are calculated for TFETs utilizing AGeNRs with different widths under a bias voltage of 0.3 V. For comparison, current-voltage characteristic of the pristine GeNR-TFET for the same ribbon width is shown as a reference.

The I-V characteristics obtained under topology (1) at the various locations for a channel having 12 and 13 atoms along the width as shown in Fig. 9(a and b). It can be seen that the presence of a defect near the source leads to a reduction of the hole current and an increase of the electron current. The presence of a defect at the mid-channel decreases the current both for the electron and the hole. According to Fig. 9(a and b), due to the presence of a defect near the drain, an increase in the hole current and a decrease in the electron current are observed. Also, the minimum current indicates a slight increase in all cases. We know TFETs

exhibit ambipolar characteristics. Note that the ambipolar characteristic in the TFETs comes from the fact that by applying the high (low) gate voltage, the electron (hole) is the major carrier and the curves of these devices are 'V' shape. Despite the defect locations in the structure, in all the cases the 'V' shape of current-voltage characteristics is preserved.

The current characteristics under the influence of antidote defect type (2) at the designated locations in the channel for widths of 12 and 13 is shown in Fig. 10(a and b).

According to Fig. 10(a) which belongs to width of 12 atoms, the presence of a defect in the mid-channel has damaged the current characteristics. Also, a dramatic increase of the current around the Dirac point is observed that has led to the destruction of 'V' shape characteristic. When the antidote defect is located close to the source, both electron and hole currents are decreased. However, the hole current has decreased more than the electron current. In addition, the minimum current has not changed. According to Fig. 10(a), the presence of defects near the drain causes the electron current to be reduced and the hole current increases corresponding to the left branch of the curve. The minimum current has also increased. The other result is that the Dirac point drifts to a higher or lower voltage due to presence of antidote defects near the drain and source, respectively. At the Dirac point, the electron and hole currents become equal and thus, the minimum current in the I-V characteristic is created. By the presence of a defect in the

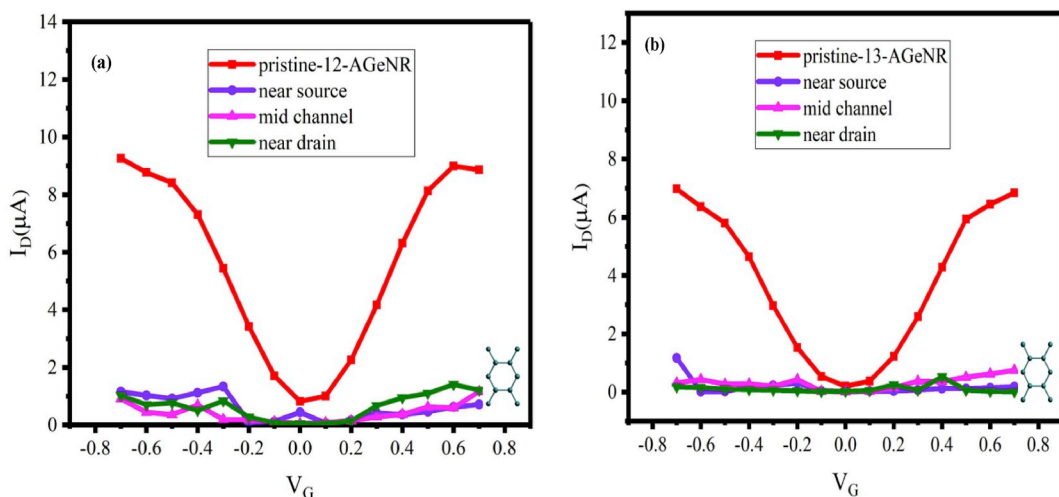


**Fig. 11.** Current-voltage characteristics of AGeNR-TFET subject to topology 3 antidote defect at different locations in the channel; (a)  $N = 12$  (b)  $N = 13$ .

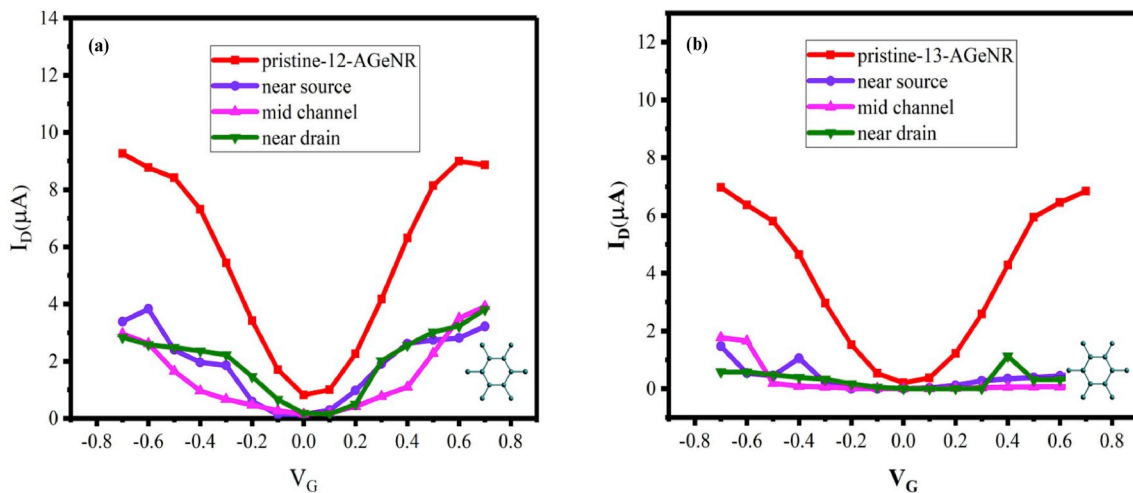


**Fig. 12.** Current-voltage characteristics of AGeNR-TFET subject to topology 4 antidote defect at different locations in the channel; (a)  $N = 12$  (b)  $N = 13$ .

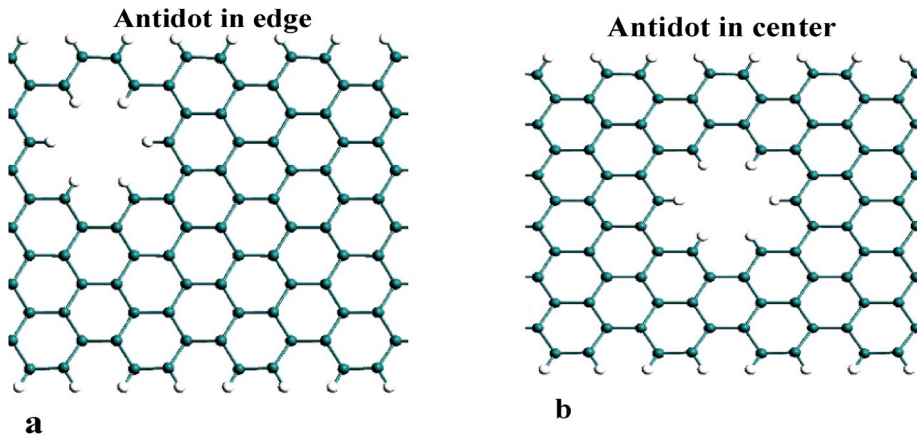


**Fig. 13.** Top views of the optimized structures for defected 12-AGeNR: (a) antidote at the edge (b) antidote at the center.

structure, the electron and hole current components at the Dirac point are imbalanced. Therefore, both currents should be balanced to reach Dirac point. Since the hole (electron) current decreases due to the presence of a defect near the source(drain), it is necessary to enhance the hole (electron) current by decreasing (increasing) the gate voltage to reach the Dirac point. Furthermore, despite the presence of this type of defects near the source or drain, the 'V' shape of current-voltage characteristics is preserved.

Fig. 10(b) illustrates the previous analysis for width of 13 atoms along the GeNR. It is observed that the presence of a defect close the source decreases the current. Moreover, electrons current has decreased more than the hole current. When the defect is located close to the drain, both of the currents are decreased and the hole current is reduced more than electron current. When the defect is placed in the middle of the channel, both hole and electron currents are reduced. Also, the minimum current in all three cases is reduced compared with the pristine case but the 'V' shape of the characteristic is preserved at all three locations.

In Fig. 11(a and b) the current-voltage characteristics is shown under the antidote of topology(3) at different locations in the channel. According to Fig. 11(a and b), both the channel current and the minimum current are remarkably reduced compared with the pristine structure. The 'V' shape of the current-voltage characteristics for widths of 12 and 13 are destroyed.

In Fig. 12(a and b) the current-voltage characteristics are shown

under the antidote of topology(4) at different locations in the channel. According to this figure, both of them emphasize a reduction of the channel current and the minimum current. Also the 'V' shape of the transfer characteristics for width of 12 atoms is maintained although it is destroyed for width of 13 atoms.

According to the obtained current-voltage characteristics in Figs. 9–12, it is seen that only antidote of kind topology 1 outperforms the pristine nanoribbons when it is utilized in the channel of TFET. This is caused by enhanced drive current ( $I_{on}$ ) and reduced ambipolar current ( $I_{amb}$ ) particularly when the antidote is located close to the source.

It should be noted that in all of the previous simulations, the antidote position was varied in the lateral position. In other words, we assumed all kinds of antidotes are positioned in the center of supercells shown in Fig. 1 to maintain the structure symmetry. To investigate the electronic properties and current-voltage characteristics when the positions of antidotes change in the transverse direction, we carried out further simulation for  $N = 12$  and antidotes of topology 1. As shown in Fig. 13, two different positions are assumed for antidotes: (a) at the edge of the supercell, (b) at the center of the supercell. Fig. 14 displays the influence of these transverse positions on the band structure of the supercell. As can be seen, when the antidote vacancy is placed on the edge of the supercell, the bandgap is changed and its value is larger than the case when the antidote is positioned in the center of the supercell.

Fig. 15 indicates I–V characteristics under topology 1 for the same locations in the transverse direction. As can be seen in Fig. 15(a), with

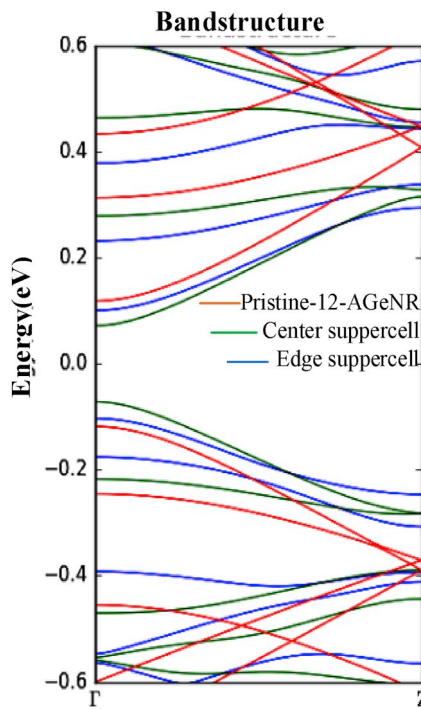


**Fig. 14.** Energy band structure of AGeNR for pristine and defective with antidotes of topology 1 in center and edge of the supercell for  $N = 12$ .

the antidote position is varied from the center to the edge, very slight change is observed in the current behavior. Also the presence of a defect in the middle of the channel and at the edge position caused the channel current to be decreased relative to the center position, but the minimum current does not change, as seen in Fig. 15(b). Fig. 15(c) shows that when the defect is near the drain and at the edge position, a significant amount of decrease in the channel current relative to the center position is observed, particularly at more negative gate voltages.

It is worth noting that we have divided the channel into three supercells: two perfect supercell (like Fig. 1) and one defective supercell (like Fig. 13). For instance, in order to study the impact of lateral position when the defect is close to the source, the defected supercell is assumed connected to the source electrode, one perfect supercell is assumed to be in the middle, and another perfect electrode is assumed to be connected to the drain.

In order to investigate the output characteristics of the devices under study, we calculated current variation versus the bias voltage at  $V_G = 0.4$  V. The applied bias voltage varied from 0 to 2 V. Fig. 16 shows this

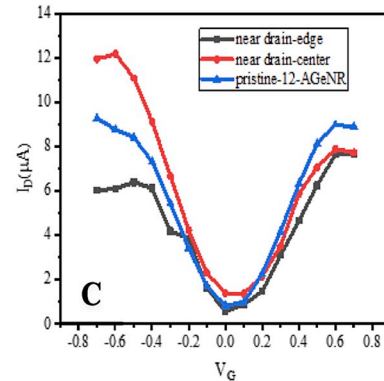
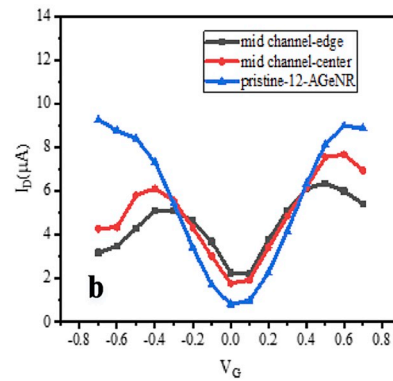
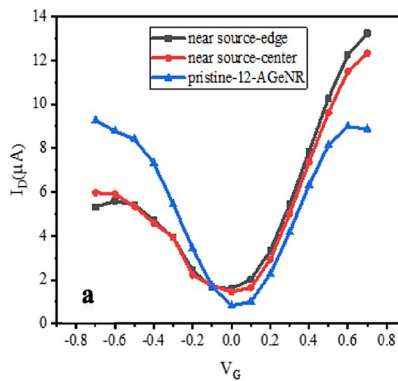


**Fig. 15.** Current-voltage characteristics of AGeNR-TFET subject to topology 1 antidote defect at different locations in the channel at the two positions of the center and the edge; (a) near source (b) mid channel (c) near drain.

characteristics for two cases corresponding to pristine device and the device with antidote of topology 1. It is worth noting that the negative differential resistance which can be seen in some atomic scale systems [46], is not seen neither in pristine nor in the device with antidote. Moreover, the device with antidote topology 1 presents slightly more current compared with pristine case.

#### 4. Conclusion

In this article, we comprehensively studied the impact of four categories of antidote vacancies on the electronic properties and the current-voltage characteristics of armchair germanene nanoribbons using a combination of DFT and non-equilibrium Green's function (NEGF) method.

The results showed that defective ribbons depending on the type of topologies and the ribbon width, illustrate different behaviors. Depending on the defect topology, the bandgap size can be increased or decreased. It was shown that the presence of defects causes the electronic properties to be altered from semiconducting to metallic and vice versa. The ambipolar behavior was significantly affected. Moreover, the presence of antidote defects in the channel affects the transfer characteristics by reduction or increase of the total current and drift of the Dirac point.

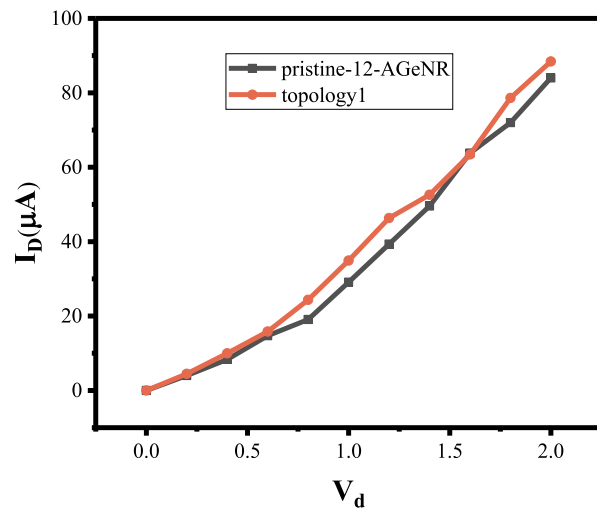


**Fig. 16.** Comparison of output characteristics between pristine and one defective structure.

## Declaration of competing interest

The authors declare that they have no known competing financial interests or personal relationships that could have appeared to influence the work reported in this paper.

## Acknowledgements

This research was supported by University of Kashan under supervision of Dr. Daryoosh Dideban. Authors are thankful to the support received for this work from Microelectronics Lab (meLab) at the University of Glasgow, UK.

## References

- [1] S. Chang, Y. Zhang, Q. Huang, H. Wang, G. Wang, Effects of vacancy defects on graphene nanoribbon field effect transistor, *Micro & Nano Lett.* 8 (2013) 816–821.
- [2] M. Zoghi, A.Y. Goharrizi, M. Saremi, Band gap tuning of armchair graphene nanoribbons by using antidotes, *J. Electron. Mater.* 46 (2017) 340–346.
- [3] M. Zoghi, A.Y. Goharrizi, The electronic properties of armchair graphene nanoribbons defected by hexagonal antidotes and boron/nitride atoms, in: 2017 Iranian Conference on Electrical Engineering (ICEE), 2017, pp. 355–359.
- [4] W. Tian, Y. Zeng, Z. Zhang, Electronic properties of graphene nanoribbons with periodically hexagonal nanoholes, *J. Appl. Phys.* 114 (2013), 074307.
- [5] M.B. Tagani, Electrical and mechanical properties of a fully hydrogenated two-dimensional polyaniiline sheet, *Comput. Mater. Sci.* 153 (2018) 126–133.
- [6] G. Berdiyorov, F. Peeters, Influence of vacancy defects on the thermal stability of silicene: a reactive molecular dynamics study, *RSC Adv.* 4 (2014) 1133–1137.
- [7] L.E.F. Torres, S. Roche, J.-C. Charlier, *Introduction to Graphene-Based Nanomaterials: from Electronic Structure to Quantum Transport*, Cambridge University Press, 2014.
- [8] A.Y. Goharrizi, Resonant tunneling diode by means of compound armchair boron/nitride and graphene nanoribbons, *J. Electron. Mater.* 48 (2019) 1235–1242.
- [9] A.Y. Goharrizi, M. Zoghi, M. Saremi, Armchair graphene nanoribbon resonant tunneling diodes using antidote and BN doping, *IEEE Trans. Electron Devices* 63 (2016) 3761–3768.
- [10] Z.T. Esfahani, A. Saffarzadeh, A. Akhound, A DFT study on the electronic and magnetic properties of triangular graphene antidot lattices, *Eur. Phys. J. B* 91 (2018) 308.
- [11] H. Chen, K.-H. Jin, H. Guo, B. Wang, A.O. Govorov, X. Niu, et al., Nanoperforated graphene with alternating gap switching for optical applications, *Carbon* 126 (2018) 480–488.
- [12] K. Iordanidou, M. Houssa, B. van den Broek, G. Pourtois, V. Afanas'ev, A. Stesmans, Impact of point defects on the electronic and transport properties of silicene nanoribbons, *J. Phys. Condens. Matter* 28 (2016), 035302.
- [13] S. Mehdi Aghaei, I. Calizo, Band gap tuning of armchair silicene nanoribbons using periodic hexagonal holes, *J. Appl. Phys.* 118 (2015) 104304.
- [14] A. Nazari, R. Faez, H. Shamloo, Modeling comparison of graphene nanoribbon field effect transistors with single vacancy defect, *Superlattice Microstruct.* 97 (2016) 28–45.
- [15] L. Yang, C.-H. Park, Y.-W. Son, M.L. Cohen, S.G. Louie, Quasiparticle energies and band gaps in graphene nanoribbons, *Phys. Rev. Lett.* 99 (2007) 186801.
- [16] Y.-W. Son, M.L. Cohen, S.G. Louie, Energy gaps in graphene nanoribbons, *Phys. Rev. Lett.* 97 (2006) 216803.
- [17] M. Saremi, M. Saremi, H. Niazi, A.Y. Goharrizi, Modeling of lightly doped drain and source graphene nanoribbon field effect transistors, *Superlattice Microstruct.* 60 (2013) 67–72.
- [18] F. Guinea, M. Katsnelson, A. Geim, Energy gaps and a zero-field quantum Hall effect in graphene by strain engineering, *Nat. Phys.* 6 (2010) 30.
- [19] J.E. Padilha, R.B. Pontes, Electronic and transport properties of structural defects in monolayer germanene: an ab initio investigation, *Solid State Commun.* 225 (2016) 38–43.
- [20] R. Balog, B. Jørgensen, L. Nilsson, M. Andersen, E. Riems, M. Bianchi, et al., Bandgap opening in graphene induced by patterned hydrogen adsorption, *Nat. Mater.* 9 (2010) 315.
- [21] F. Yavari, C. Kitzinger, C. Gaire, L. Song, H. Gulapalli, T. Borca-Tascic, et al., Tunable bandgap in graphene by the controlled adsorption of water molecules, *Small* 6 (2010) 2535–2538.
- [22] J.O. Sofo, A.S. Chaudhari, G.D. Barber, Graphane: a two-dimensional hydrocarbon, *Phys. Rev. B* 75 (2007) 153401.
- [23] M.Y. Han, B. Özylmaz, Y. Zhang, P. Kim, Energy band-gap engineering of graphene nanoribbons, *Phys. Rev. Lett.* 98 (2007) 206805.
- [24] X. Wang, Y. Ouyang, X. Li, H. Wang, J. Guo, H. Dai, Room-temperature all-semiconducting sub-10-nm graphene nanoribbon field-effect transistors, *Phys. Rev. Lett.* 100 (2008) 206803.
- [25] S. Singh, K. Garg, A. Sareen, R. Mehla, I. Kaur, Doped armchair germanene nanoribbon exhibiting negative differential resistance and analysing its nano-FET performance, *Org. Electron.* 54 (2018) 261–269.
- [26] Z. Ni, Q. Liu, K. Tang, J. Zheng, J. Zhou, R. Qin, et al., Tunable bandgap in silicene and germanene, *Nano Lett.* 12 (2011) 113–118.
- [27] H.-C. Wu, A.N. Chaika, T.-W. Huang, A. Syrlybekov, M. Abid, V.Y. Aristov, et al., Transport gap opening and high on-off current ratio in trilayer graphene with self-aligned nanodomain boundaries, *ACS Nano* 9 (2015) 8967–8975.
- [28] L. Ci, L. Song, C. Jin, D. Jariwala, D. Wu, Y. Li, et al., Atomic layers of hybridized boron nitride and graphene domains, *Nat. Mater.* 9 (2010) 430.
- [29] B. Xu, Y. Lu, Y. Feng, J. Lin, Density functional theory study of BN-doped graphene superlattice: role of geometrical shape and size, *J. Appl. Phys.* 108 (2010), 073711.
- [30] H. Zhu, K. Suenaga, A. Hashimoto, K. Urata, S. Iijima, Structural identification of single and double-walled carbon nanotubes by high-resolution transmission electron microscopy, *Chem. Phys. Lett.* 412 (2005) 116–120.
- [31] M. Topsakal, E. Aktürk, H. Sevinçli, S. Ciraci, First-principles approach to monitoring the band gap and magnetic state of a graphene nanoribbon via its vacancies, *Phys. Rev. B* 78 (2008) 235435.
- [32] S. Cahangirov, M. Topsakal, E. Aktürk, H. Şahin, S. Ciraci, Two-and one-dimensional honeycomb structures of silicon and germanium, *Phys. Rev. Lett.* 102 (2009) 236804.
- [33] H. Şahin, S. Cahangirov, M. Topsakal, E. Bekaroglu, E. Aktürk, R.T. Senger, et al., Monolayer honeycomb structures of group-IV elements and III-V binary compounds: first-principles calculations, *Phys. Rev. B* 80 (2009) 155453.
- [34] S.Z. Butler, S.M. Hollen, L. Cao, Y. Cui, J.A. Gupta, H.R. Gutierrez, et al., Progress, challenges, and opportunities in two-dimensional materials beyond graphene, *ACS Nano* 7 (2013) 2898–2926.
- [35] P. Bandaru, P. Pichanusakorn, An outline of the synthesis and properties of silicon nanowires, *Semicond. Sci. Technol.* 25 (2010), 024003.
- [36] S. Balendhran, S. Walia, H. Nili, S. Sriram, M. Bhaskaran, Elemental analogues of graphene: silicene, germanene, stanene, and phosphorene, *Small* 11 (2015) 640–652.
- [37] T.-T. Jia, X.-Y. Fan, M.-M. Zheng, G. Chen, Silicene nanomeshes: bandgap opening by bond symmetry breaking and uniaxial strain, *Sci. Rep.* 6 (2016) 20971.
- [38] S. Li, Y. Wu, Y. Tu, Y. Wang, T. Jiang, W. Liu, et al., Defects in silicene: vacancy clusters, extended line defects, and di-adatoms, *Sci. Rep.* 5 (2015) 7881.
- [39] T.G. Pedersen, C. Flindt, J. Pedersen, N.A. Mortensen, A.-P. Jauho, K. Pedersen, Graphene antidot lattices: designed defects and spin qubits, *Phys. Rev. Lett.* 100 (2008) 136804.
- [40] X. Cui, L. Li, R. Zheng, Z. Liu, C. Stampfl, S.P. Ringer, Graphene based dots and antidots: a comparative study from first principles, *J. Nanosci. Nanotechnol.* 13 (2013) 1251–1255.
- [41] A.H. Bayani, et al., Impact of uniaxial compressive strain on physical and electronic parameters of a 10 nm germanene nanoribbon field effect transistor, *Superlattice Microstruct.* 100 (2016) 198–208.
- [42] H. Fatholahnejad, et al., Tuning the analog and digital performance of Germanene nanoribbon field effect transistors with engineering the width and geometry of source, channel and drain region in the ballistic regime, *Mater. Sci. Semicond. Process.* 80 (2018) 18–23.
- [43] VNL-ATK is a licensed software which can be accessed, from, <https://docs.quantumwise.com/v2016/>.
- [44] S. Kaneko, H. Tsuchiya, Y. Kamakura, N. Mori, M. Ogawa, Theoretical performance estimation of silicene, germanene, and graphene nanoribbon field-effect transistors under ballistic transport, *APEX* 7 (2014), 035102.
- [45] M. Monshi, S. Aghaei, I. Calizo, Edge functionalized germanene nanoribbons: impact on electronic and magnetic properties, *RSC Adv.* 7 (2017) 18900–18908.
- [46] S.A. Tawfik, et al., Enhanced oscillatory rectification and negative differential resistance in pentamantane diamondoid-cumulene systems, *Nanoscale* 8 (6) (2016) 3461–3466.